46th AIAA/ASME/SAE/ASEE Joint Propulsion Conference & Exhibit
25 - 28 July 2010, Nashville, TN

AIAA 2010-6765

On the Viscous Bidirectional Vortex. Part 3: Multiple Mantles

Joshua W. Batterson* and Joseph Majdalani†
University of Tennessee Space Institute, Tullahoma, TN 37388, USA

This study seeks to characterize the multiple flow reversals that may arise in the context of bidirectional vortex motion. It constitutes an essential sequel to the analysis of the linear and nonlinear Beltramian motions wherein the formation of only one mantle is considered. The mantle in cyclonic flows refers to the non-translating interface separating the updraft from the downdraft. In this work, we show that an odd number of mantles may develop and these are accompanied by endwall flow reversals that may be predicted by sequentially higher eigenvalues derived directly from first principles. The multiplicity of mantle alignments is corroborated by experimental measurements obtained in swirl-driven vortex chambers. The resulting flowfield is characterized by multilayered coaxial vortex shells with sign-alternating axial velocity. In this article, the multiple solutions associated with different modes of flow reversal are ascertained using as a baseline, each of the linear and nonlinear Beltramian motions obtained by Majdalani (Majdalani, J., "Exact Eulerian Solutions of the Cylindrical Bidirectional Vortex," AIAA Paper 2009-5307, Denver, Colorado, Aug. 2009). Our analytical approximations are shown to predict the positioning of internal mantles with substantial accuracy when compared to computational fluid dynamics (CFD) and experimental particle-image velocimetry (PIV) data. In addition, viscous layers that appear in the core and sidewall regions are quantified and appended to the inviscid models as required.

Nomenclature

A_i	=	inlet area
B	=	tangential angular momentum, ru_θ
H	=	total stagnation pressure head, $p + \frac{1}{2}u^2$
Q_i	=	nondimensional volumetric flow rate, $\bar{Q}_i/(Ua^2)$
Re	=	injection Reynolds number, $Ua/\nu = 1/\varepsilon$
S	=	swirl number, $\pi ab/A_i = \pi\beta\sigma$
U	=	average inflow velocity in the tangential direction, $\bar{u}_\theta(a, L)$
V	=	vortex Reynolds number, $Q_i Re(a/L) = (\varepsilon\sigma l)^{-1} = 2\pi\kappa/\varepsilon$
$\bar{Q}_i$	=	inlet volumetric flow rate
$\boldsymbol{u}$	=	nondimensional velocity, $(\bar{u}_r, \bar{u}_\theta, \bar{u}_z)/U$
a	=	chamber radius
b	=	chamber outlet radius
l	=	chamber aspect ratio, L/a
p	=	nondimensional pressure, $\bar{p}/(\rho U^2)$
r, z	=	nondimensional radial and axial coordinates, $(\bar{r}, \bar{z})/a$
s	=	scaled radial coordinate

Subscripts

0	=	reference value at the chamber headwall
θ	=	tangential component
c	=	represents a solution in the core
i	=	inlet property
m	=	mode number
r, z	=	radial or axial component
w	=	represents a solution near the wall

*Graduate Research Assistant, Mechanical, Aerospace and Biomedical Engineering Department. Student Member AIAA.
†H. H. Arnold Chair of Excellence in Advanced Propulsion, Mechanical, Aerospace and Biomedical Engineering Department. Senior Member AIAA. Fellow ASME.

Symbols

α = constant, $\frac{\lambda_0}{2\beta J_1(\lambda_0\beta)}\left(\frac{1}{8}\lambda_0^2 - 1\right)$
β = normalized outlet radius, b/a
δ = characteristic boundary layer thickness
δ_p = location of maximum pressure gradient
ϵ = viscous parameter, $1/Re = \nu/(Ua)$
γ = constant, $\frac{\lambda_0}{4\beta J_1(\lambda_0\beta)}$
κ = inflow parameter, $Q_i/(2\pi l) = (2\pi\sigma l)^{-1}$
λ = eigenvalue
ν = kinematic viscosity
ω_f = constant angular speed of the forced vortex
$\boldsymbol{\omega}$ = vorticity vector
ψ = streamfunction
ρ = density
σ = modified swirl number, $Q_i^{-1} = S/(\pi\beta)$
υ = separation constant

Superscripts

$\bar{}$ = overbars denote a dimensional variable
c = denotes a composite solution
ci = denotes a composite-inner solution
i = denotes an inner solution
o = denotes an outer solution
w = denotes a near-wall solution

I. Introduction

Heat exchangers promote the transfer of energy between two mediums and are often designed in a variety of geometric configurations and conceptual arrangements.[1] These include widely used platforms such as the shell-and-tube, plate-and-frame, crossflow, and counterflow patterns with either single or multiple passes.[2] Depending on the geometric scale and configuration at hand a finite number of passes, such as 3-4, is typically pursued for optimal performance. The same may be said of the analogous problem arising in the vortex-fired rocket engine flowfield where the onset of multiple passes can be helpful in promoting better mixing and combustion efficiency between the fuel and oxidizer mediums, prolonged particle trajectory and fuel residence time,[3,4] and in the case of the internally-cooled liquid thrust chamber, more effective thermal shielding.[5]

Thus it may be seen that, in the propulsion community, a new category of vortex-fired engines is emerging in which the unique properties of cyclones are leveraged. Examples encompass both the Vortex Injection Hybrid Rocket Engine (VIHRE) and the Vortex Combustion Cold-Wall Chamber (VCCWC). These types of hybrid and liquid thrust chambers have been undergoing development by Gloyer, Knuth and Goodman,[3] Knuth *et al.*,[4] and Chiaverini *et al.*[5] The corresponding vortex engines comprise swirl-dominated combustion chambers in which different types of bidirectional vortex motions may be established. The simplest bidirectional vortex pattern allows the flow entering upstream of the base, usually an oxidizer, to travel straight to the headwall, reverse polarity while turning inwardly, and then traverse the chamber length a second time in the direction of the nozzle. A multidirectional flowfield such as the one envisioned here repeats this process more than once while permitting the presence of secondary injection, oxidizer or fuel, at either endwalls, fore or aft. The additional layering that accompanies such configuration leads to a tight confinement of the heated combustion products in an inner vortex tube that, in turn, remains separated from the chamber walls by virtue of concentric annular layers of fluid. Evidently, such an arrangement stands to provide improved thermal protection and internal chamber cooling. A multidirectional flowfield, such as the one depicted in Fig. 1, can further increase the residence time of combustion products and, in the process, induce higher combustion efficiencies.

Chronologically, the inception of the VCCWC prototype prompted the investigation by Vyas and Majdalani[6] that led to the first three-dimensional, axisymmetric, complex-lamellar, Eulerian model to describe the motion of confined cyclones. Majdalani[7] later employed the Bragg-Hawthorne equation to derive two inviscid Beltramian solutions

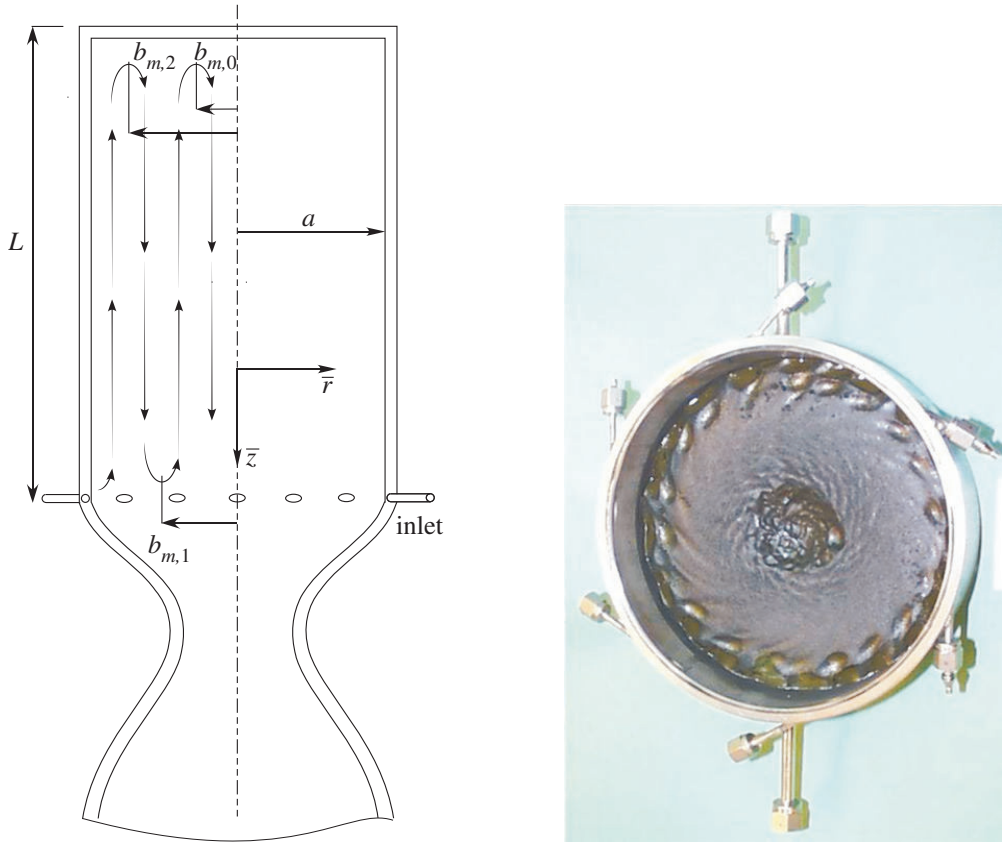

Figure 1. Here we show a) the VCCWC configuration including the coordinate system used and several mantle stations, and b) the injector faceplate of an experimental end-burning hybrid grain with multiple grooves caused by multidirectional vortex motion.

comprising either linear or nonlinear spatial dependence. In the interim, experimental and numerical evidence gathered by Anderson *et al.*,[8] Rom, Anderson and Chiaverini,[9] and others have corroborated the existence of interchanging flow reversals. The presence of multi-layering was further substantiated by the higher eigensolutions stemming from Vyas and Majdalani's complex-lamellar model.[10] Besides the VCCWC configuration, systems such as the Vortex Hybrid Engine by Gloyer, Knuth and Goodman,[3] the Vortex Injection Hybrid Rocket Engine by Knuth *et al.*,[4] and the Reverse Vortex Combustor (RVC) by Matveev *et al.*[11] have been known to exhibit the basic configuration requirements for multidirectional vortex flows. The present work will hence devote itself to the mathematical and physical arguments associated with the formation of multiple mantles. Our point of departure will be the family of three-dimensional, axisymmetric, Beltramian profiles with small viscosity at the core and sidewall boundary. The analysis will constitute a sequel to the two studies by the authors[12,13] in which the boundary layers of the linear and nonlinear Beltramian models are separately treated. A similar asymptotic procedure will be employed here to overcome the essential singularities connected with a purely inviscid, multidirectional, Beltramian vortex. In this vein, the centerline singularity will be treated along with the three-dimensional boundary layers that develop at the sidewall. Unlike the complex-lamellar vortex that has necessitated a separate asymptotic analysis to resolve its core and sidwall boundary layers, we find the viscous corrections of the Beltramian model to mirror those constructed for the case of one mantle.

II. Linear Beltramian Motion with Multiple Mantles

It may be recalled that the solution of the Beltramian model with linear spatial dependence leads to a streamfunction of the form[7]

$$\psi = \psi_0 z r J_1(\lambda_m r) \tag{1}$$

where λ_m is a placeholder for the roots of the Bessel function of the first kind. These are given by

$$\lambda_m = \{3.83171, 7.01559, 10.1735, 13.3237, \cdots\}. \tag{2}$$

Whereas the use of $\lambda_0 = 3.83171$ may be associated with single mantle formation, each consecutive eigenvalue will give rise to one additional flow reversal. For propulsive applications we require the flow to exit at the aft end of the chamber. Only even eigenvalues with $m = 0, 2, 4, \ldots$ may therefore be considered lest an unphysical setting with implausible inflow and outflow boundary conditions is engendered.

To determine the last constant ψ_0 in Eq. (1), we apply the volume conservation principle by insisting that all injected flow be evacuated through the exit port. This enables us to deduce the last constant and thereby achieve closure through

$$Q_i = \int_0^{\beta_{m,0}} \int_0^{2\pi} \boldsymbol{u}(r,l) \cdot \boldsymbol{n}\, r\, \mathrm{d}r = 2\pi \int_0^{\beta_{m,0}} u_z(r,l) r\, \mathrm{d}r = 2\pi \int_0^{\beta_{m,0}} \frac{1}{r} \frac{\partial \psi(r,l)}{\partial r}\, r\, \mathrm{d}r \tag{3}$$

and so

$$\psi_0 = Q_i / [2\pi l \beta_{m,0} J_1(\lambda_m \beta_{m,0})]. \tag{4}$$

The solution for multiple mantles may hence be reproduced from

$$\psi = \kappa z r \frac{J_1(\lambda_m r)}{\beta_{m,0} J_1(\lambda_m \beta_{m,0})} \tag{5}$$

where $\kappa = Q_i/(2\pi l)$.

For an ideal configuration in which no collisions occur during outflow, the exit port radius may be chosen in such a way to match the position of the innermost mantle, for any given flow reversal mode number, m. The flow configuration associated with each increasing eigenvalue may be linked to a progressively shorter mantle radius, $\beta_{m,0}, \{m = 0, 2, 4, \cdots\}$. For a fixed reversal mode number m, the locations of all internal mantles $\beta_{m,n}, \{n = 0, 1, \cdots, m\}$ may be extracted from the roots of $J_0(\lambda_m \beta_{m,n}) = 0$ and catalogued in Table 1. Results show both $\beta_{m,n}$ and λ_m from one to eleven internal mantles. It can thus be seen that the radius of the innermost mantle decreases precipitously from 0.628 in a single mantle configuration to 0.236, 0.146, and 0.106 in the case of two, four, and six mantles. Obviously, as in the case of heat exchangers, smaller outlet radii or larger flow reversal mode numbers may be impractical and may lead to unphysical behavior.

With the advent of the streamfunction, the tangential velocity may be readily obtained using $B = \sqrt{\lambda_m^2 \psi^2 + B_1}$. The axial and radial velocities may be similarly obtained directly from the streamfunction. The last remaining constant B_1 may be deduced from the tangential velocity requirement at entry, $u_\theta(1, l) = 1$. This condition compels the tangential velocity to match the injection velocity at the endwall. The ensuing representation for the inviscid velocity becomes

$$\boldsymbol{u} = -\kappa \frac{J_1(\lambda_m r)}{\beta_{m,0} J_1(\lambda_m \beta_{m,0})} \boldsymbol{e}_r + r^{-1} \sqrt{1 + \frac{\lambda_m^2 \kappa^2 r^2 z^2 J_1^2(\lambda_m r)}{{\beta_{m,0}}^2 J_1^2(\lambda_m \beta_{m,0})}}\, \boldsymbol{e}_\theta + \lambda_m \kappa z \frac{J_0(\lambda_m r)}{\beta_{m,0} J_1(\lambda_m \beta_{m,0})} \boldsymbol{e}_z \tag{6}$$

It should be noted that, in the absence of friction, no deceleration in the tangential velocity may occur. Instead, slippage at the sidewall will permit the swirling speed to remain constant, i.e., $u_\theta(1, z) = 1$, along the entire length of the chamber, $0 \le z \le l$. To overcome this deficiency, a viscous boundary layer treatment is required.

Table 1. Eigenvalues and corresponding mantle locations for even flow reversal mode numbers and an odd number of internal mantles

m	λ_m	$\beta_{m,0}$	$\beta_{m,1}$	$\beta_{m,2}$	$\beta_{m,3}$	$\beta_{m,4}$	$\beta_{m,5}$	$\beta_{m,6}$	$\beta_{m,7}$	$\beta_{m,8}$	$\beta_{m,9}$	$\beta_{m,10}$
0	3.832	0.628										
2	10.174	0.236	0.543	0.851								
4	16.471	0.146	0.335	0.525	0.716	0.907						
6	22.760	0.106	0.243	0.380	0.518	0.656	0.794	0.932				
8	29.047	0.083	0.190	0.298	0.406	0.514	0.622	0.730	0.838	0.947		
10	35.332	0.068	0.156	0.245	0.334	0.423	0.511	0.600	0.689	0.778	0.867	0.956

A. Viscous Corrections

The inviscid velocity is marred by two physical defects, both attributable to the absence of viscosity. Firstly, an essential singularity in the tangential velocity is observed at the centerline. Secondly, viscous interactions of the flow with the sidewall are discounted in all three vector directions. In Part 1 of this series,[12] the necessary viscous corrections are obtained for the linear, bidirectional model. After some effort, it may be realized that the same findings and flow characteristics in the bidirectional case may be straightforwardly conveyed to the multidirectional solution. This can be accomplished by replacing all instances of λ_0 and β by λ_m and $\beta_{m,0}$, respectively. The velocity for multiple mantles becomes

$$\begin{aligned}\boldsymbol{u} = -\frac{\kappa J_1(\lambda_m r)}{\beta J_1(\lambda_m \beta_{m,0})}\left[1 - e^{-\frac{V}{2\pi}\alpha(1-r)}\right]\boldsymbol{e}_r \\ + \frac{1}{r}\left[\left(1 + \frac{\lambda_m^2\kappa^2 r^2 z^2 J_1^2(\lambda_m r)}{\beta_{m,0}^2 J_1^2(\lambda_m\beta_{m,0})}\right)^{1/2} - e^{-\frac{V}{2\pi}\gamma r^2} - e^{-\frac{V}{2\pi}\alpha(1-r)}\right]\boldsymbol{e}_\theta \\ + \frac{\lambda_m \kappa z J_0(\lambda_m r)}{\beta_{m,0} J_1(\lambda_m\beta_{m,0})}\left[1 - e^{-\frac{V}{2\pi}\alpha(1-r)}\right]\boldsymbol{e}_z \quad (7)\end{aligned}$$

where $\alpha = \lambda_m\left(\frac{1}{8}\lambda_m^2 - 1\right)/[2\beta_{m,0}J_1(\lambda_m\beta_{m,0})]$ and $\gamma = \lambda_m/[4\beta_{m,0}J_1(\lambda_m\beta_{m,0})]$.

B. Tangential Velocity

The tangential velocity corrections incorporate viscous effects near the centerline and along the sidewall. Friction around the centerline leads to a forced core vortex, thus eliminating the unbounded behavior seen in the inviscid model. In the core of the forced vortex, the velocity is directly proportional to the radial distance from the centerline. Near the sidewall, a thin boundary layer is established that is highly dependent on the vortex Reynolds number, $V = Q_i Re(a/L) = (\varepsilon\sigma l)^{-1} = 2\pi\kappa/\varepsilon$.

In Fig. 2 the tangential velocity corresponding to multiple internal mantles is characterized vis-à-vis variations in z and V. Firstly in Fig. 2a, we show u_θ versus r for the case of 3 internal mantles at $z = (0.1, 0.5, 1)$ and $V = 650$. Interestingly, a small variation in the local swirl velocity is seen to accompany axial excursions. This behavior is contrary to that displayed by the axially-invariant, complex-lamellar counterpart.[6] However, consistent with our original assumptions, the z-sensitivity does not extend into the viscous regions. Secondly, by shifting our attention to Fig. 2b, it may be seen that when the vortex Reynolds number is increased from 200 to 800, a corresponding reduction in the core layer is entailed. This behavior is consistent with Prandtl's classic theory. Figure 2b clearly shows a sequential decrement in the depth of penetration into the bulk fluid and a larger $(u_\theta)_{\max}$ with increasing V. Thirdly, increasing the flow reversal mode number from 0 to 4 is showcased in Fig. 2c where the behavior of u_θ is illustrated with one, three, and five internal mantles. Increasing the number of mantles has a similar effect to that of increasing V. It naturally leads to a narrower forced vortex core, a wider inviscid segment, thinner boundary layers, and higher swirl velocities. Given the scale on the graph, the appreciable reduction in wall layer thickness that accompanies successive increases in m is not visible. A magnification of the sidewall region, which is furnished in Fig. 2d, clearly shows the substantial depreciation in the boundary layer region while increasing the number of internal mantles. The relatively sharp turning observed at higher modes is due to the thinning of the boundary layer which, for the complex-lamellar case, scales with $(m+1)^{-3}$. This effect will be further elaborated in the upcoming discussion of the axial velocity.

C. Axial Velocity

Because the zeroes of u_z define the mantle stations, an examination of the axial velocity clarifies the effects of multiple flow reversals. In this vein, Figs. 3a and 3c illustrate the linear dependence of the solution on the axial position. As usual, we keep $V = 650$ and plot u_z at $z = \{0.1, 0.5, 1\}$. Because the outer solution remains linearly dependent on the axial coordinate, we continue to observe proportionately higher axial speeds at progressively larger axial distances with the maximum u_z occurring in the exit plane. Multidirectional flow effects are described in Fig. 3b where the axial velocity is plotted for the first three even mode numbers. Beyond incorporating multiple flow reversals, the higher centerline velocities are also caused by an increased value of m. As in the case of the complex-lamellar model, sequential increases in m lead to a smaller outlet radius and hence a higher axial velocity is required to permit the same mass flow rate in exiting the chamber. Visually, Fig. 3b shows that the addition of viscosity is significantly

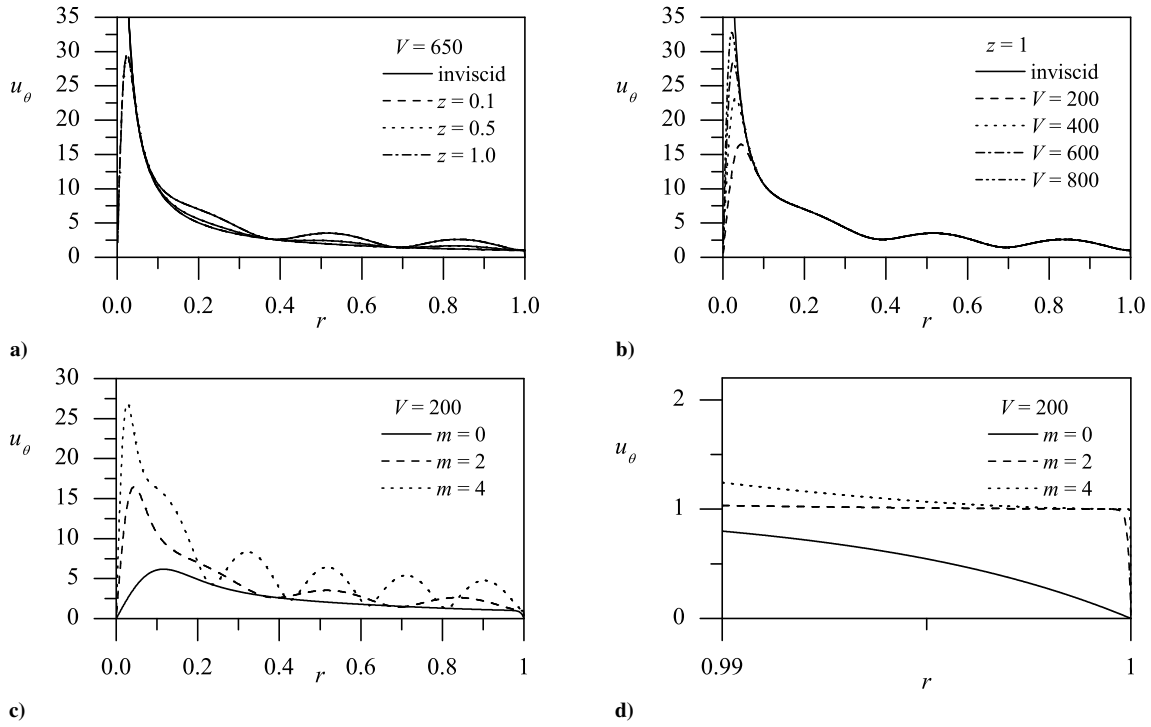

Figure 2. Tangential velocity plots with 3 mantles ($m = 2$) showing the effects of a) axial variations and b) sequentially increasing V. In Part c) and its magnified sidewall region in d) we show the effects of sequentially increasing the flow reversal mode number at fixed $z = 1$. Unless stated otherwise, we use $\kappa = 0.103$ everywhere.

overshadowed by the effect of the mode number. As one may expect, the viscous corrections only impact the mantle nearest to the wall with minimal influence on its maximum velocity. Higher mode numbers result in the development of thinner vortex tubes near the sidewall, thus causing the boundary layers to shrink accordingly. This result is displayed graphically in Fig. 3d and posted numerically in Table 3. Before leaving this section, we note that the limiting case of $V \to 0$ is connected with the inflow parameter $\kappa \to 0$. So as one would expect, the absence of a mean inflow velocity causes the solution to categorically vanish. Conversely, by setting $V \to \infty$ in Eq. (7), the inviscid baseline model is swiftly recovered.

D. Radial Velocity

The radial velocity alternates direction largely due to its strong connection with the axial flow profile through continuity. The resulting distribution allows for both positive and negative, therefore inward and outward motions across concentric mantles. From the standpoint of VCCWC performance, this type of recirculation and mass exchange may further increase the residence time of reacting products and thus improve combustion efficiency. As for the viscous corrections in the radial velocity, they are consistently found to be of second order. Despite our retention of the mathematical form underlying both tangential and axial boundary layers, the asymptotic treatment of u_r leads to minor adjustments in the slope at the wall. This result may be viewed in Fig. 4 where u_r is described for $m = 0, 2, 4$. Unlike the visible effect of m on u_r, variations in V are confined to the thin wall layer. The latter leads to smooth viscous tempering whereby the velocity and its derivative gradually approach zero at the sidewall.[12–14] This effect is corroborated in the numerical work of Morgan,[15,16] Blasius,[17] and others. As it may be seen in Fig. 4b, the second order effects are further diminished at higher mode numbers.

E. Boundary Layer Thickness

As is customary, the boundary layer thickness, δ, can be defined as the distance necessary to recover 99% of the outer solution. This definition can be applied equally well to both the forced core and sidewall regions. To

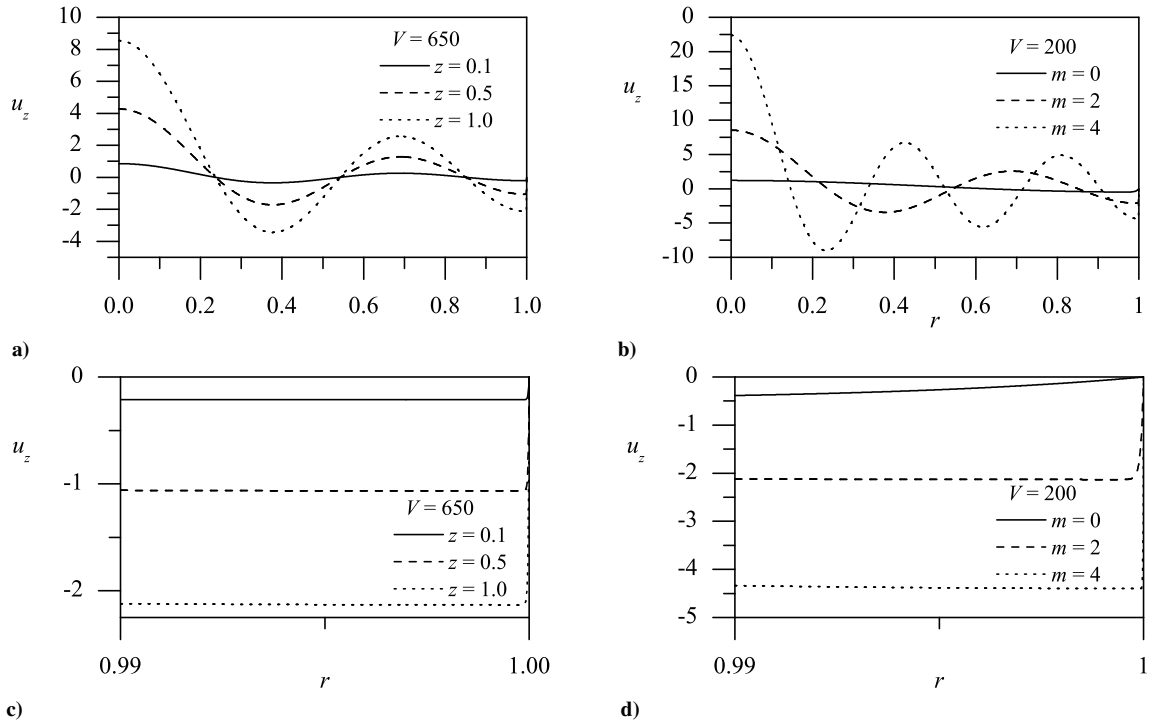

Figure 3. Axial velocity plots showing effects of a) axial variations and b) sequentially increasing V at $z = 1$. In Parts c) and d) the magnified sidewall regions are shown.

determine the viscous core thickness, δ_i, we turn our attention to Eq. (7). It is not necessary to include the tangential sidewall corrections because they do not interact with the forced core. We find that the forced core thickness must be numerically obtained from the transcendental equation

$$-\frac{V}{2\pi}\gamma r^2 = \ln\left[\frac{1}{100}\left(1+\frac{\lambda_m^2\kappa^2 r^2 z^2 J_1^2(\lambda_m r)}{\beta_{m,0}^2 J_1^2(\lambda_m \beta_{m,0})}\right)^{1/2}\right] \tag{8}$$

By taking a one-term Taylor series expansion of the preceding equation and solving directly for the radial position, an approximate analytic solution may be obtained. We find

$$\delta_i \approx \sqrt{\frac{\beta_{m,0} J_1(\lambda_m \beta_{m,0})}{2\pi z^2 \kappa^2 \lambda_m^3}\left(-V+\sqrt{V^2+64\pi^2 z^2 \kappa^2 \lambda_m^2 \ln(10)}\right)} \tag{9}$$

This solution retains a small dependence on the axial position, albeit diluted by the order of its κ^2 multiplier. Here too, the edge of the core boundary layer coincides with almost twice the radius of the forced core vortex that marks the radial distance from the centerline to the point of maximum swirl velocity.

Following similar footsteps, the sidewall boundary layer, δ_w, may be specified at the radial position where the solution reaches 99% of its inviscid value. By limiting our attention to the sidewall corrections befalling u_θ, the edge of the boundary layer may be extracted from

$$-\frac{V}{2\pi}\alpha(1-r) = \ln\left[\frac{1}{100}\left(1+\frac{\lambda_m^2\kappa^2 r^2 z^2 J_1^2(\lambda_m r)}{\beta_{m,0}^2 J_1^2(\lambda_m \beta_{m,0})}\right)^{1/2}\right] \tag{10}$$

Taking the one-term Taylor series expansion of the above and solving directly for the boundary layer's edge, one finds

$$\delta_w = 1 - r_w \approx \frac{2\pi}{V\alpha}\ln(100) \tag{11}$$

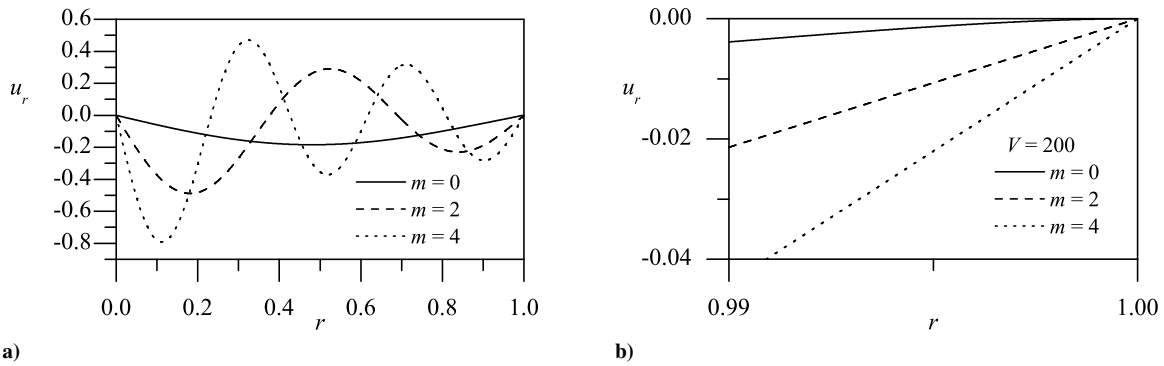

Figure 4. Radial velocity profiles at $z/l = \frac{1}{2}$ showing a) typical distribution across the chamber radius and b) magnification near the sidewall. Results correspond to flow with 1, 3 and 5 mantles.

Table 2. Prandtl's inner core and sidewall boundary layer thicknesses for the linear Beltramian model at different positions and vortex Reynolds numbers. Here $\kappa = 0.103$ and $m = 0$

	Inner boundary layer, δ_i					Sidewall boundary layer, δ_w				
z	$V = 200$	$V = 400$	$V = 600$	$V = 800$	$V = 1000$	$V = 200$	$V = 400$	$V = 600$	$V = 800$	$V = 1000$
0.0	0.2218	0.1569	0.1281	0.1109	0.0992	0.0295	0.0147	0.0098	0.0074	0.0059
0.5	0.2218	0.1569	0.1281	0.1109	0.0992	0.0295	0.0147	0.0098	0.0074	0.0059
1.0	0.2217	0.1568	0.1281	0.1109	0.0992	0.0294	0.0147	0.0098	0.0074	0.0059
1.5	0.2215	0.1568	0.1281	0.1109	0.0992	0.0294	0.0147	0.0098	0.0074	0.0059
2.0	0.2213	0.1568	0.1280	0.1109	0.0992	0.0294	0.0147	0.0098	0.0074	0.0059

This step renders the boundary layer thickness axially invariant. The maximum difference between Eq. (10) and Eq. (11) remains less than 0.2% for the range of physical parameters associated with this problem.

When this procedure is repeated for the purpose of capturing the sidewall boundary layers in either the axial or radial directions, expressions that are identical to those given by Eq. (11) are found. For a truly conforming boundary layer thickness we would expect to recover the result given in Eq. (10). This behavior is expected due to the dominance of the swirl velocity and its corresponding boundary layer thickness. The latter remains nearly invariant along the length of the chamber, thus causing both axial and radial layers to follow suit. This consistency may be seen in the typical values of δ_i and δ_w that are given in Table 2.

F. Pressure Profile

Using Euler's equations, one can easily calculate the radial and axial pressure gradients. The radial pressure gradient may be closely approximated by

$$\frac{\partial p}{\partial r} \approx r^{-3}\left(1 + e^{-\frac{V}{\pi}\gamma r^2} + e^{-\frac{V}{\pi}\alpha(1-r)} - 2e^{-\frac{V}{2\pi}\gamma r^2} - 2e^{-\frac{V}{2\pi}\alpha(1-r)}\right) + \frac{z^2\kappa^2\lambda_m^2 J_1^2(\lambda_m r)}{r\beta_{m,0}^2 J_1(\lambda_m \beta_{m,0})} \tag{12}$$

A graphical rendering of the radial gradient of pressure is furnished in Fig. 5a. Therein, one may clearly see the increasing axial sensitivity at higher flow reversal modes. The peaking radial pressure near the point of maximum swirl velocity may be attributed to the strong centrifugal action in the core region.

The pressure distribution is also showcased on this graph. In this situation, we define p_0 as the normalized pressure at the corner of the headwall. This enables us to put $\Delta p = p - p_0$. Subsequently, straightforward integration in the

Table 3. Boundary layer thickness for several mode numbers at $V = 200$ and $z = 1$

m	0	2	4
Number of internal mantles	1	3	5
Inner boundary layer thickness, δ_i	0.221701	0.083219	0.051108
Sidewall boundary layer thickness, δ_w	0.029448	0.000292	4.05E-05

radial direction renders

$$\begin{aligned}\Delta p\left(r,z\right)=&\frac{r^2-1}{2r^2}+\frac{1}{2}e^{-\frac{V}{\pi}\gamma}-e^{-\frac{V}{2\pi}\gamma}+\frac{1}{r^2}\left(e^{-\frac{V}{2\pi}\gamma r^2}-\frac{1}{2}e^{-\frac{V}{\pi}\gamma r^2}\right)\\&+\frac{V}{2\pi}\gamma\left[\mathrm{Ei}\left(-\frac{V}{\pi}\gamma\right)-\mathrm{Ei}\left(-\frac{V}{\pi}\gamma r^2\right)+\mathrm{Ei}\left(-\frac{V}{2\pi}\gamma r^2\right)-\mathrm{Ei}\left(-\frac{V}{2\pi}\gamma\right)\right]\\&+\frac{1}{2}+\frac{V}{2\pi}\alpha-\frac{V^2}{2\pi^2}\alpha^2\mathrm{Ei}\left(\frac{V}{\pi}\alpha\right)e^{-\frac{V}{\pi}\alpha}\\&+\frac{1}{2r^2\varepsilon^2}\left(-e^{-\frac{V}{\pi}\alpha(1-r)}\varepsilon\left(\varepsilon+2r\alpha\kappa\right)+4r^2\alpha^2\kappa^2e^{-\frac{V}{\pi}\alpha}\mathrm{Ei}\left(\frac{V}{\pi}\alpha r\right)\right)\\&-\frac{4\pi^2\kappa^2+2\pi\alpha V\kappa^2-\alpha^2\kappa^2\mathrm{Ei}\left(\frac{V}{2\pi}\alpha\right)e^{-\frac{V}{2\pi}\alpha}}{4\pi^2\kappa^2}\\&+\frac{\left(4\pi^2\kappa^2+2\pi V\kappa^2\alpha r\right)e^{-\frac{V}{2\pi}\alpha(1-r)}-r^2V^2\alpha^2\kappa^2e^{-\frac{V}{2\pi}\alpha}\mathrm{Ei}\left(\frac{V}{2\pi}\alpha r\right)}{4\pi^2\kappa^2r^2}\\&+\frac{z^2\kappa^2\lambda_m^2}{2\beta_{m,0}^2J_1\left(\lambda_m\beta_{m,0}\right)}\left[J_0^2\left(\lambda_m\right)-J_0^2\left(\lambda_mr\right)+J_1^2\left(\lambda_m\right)-J_1^2\left(\lambda_mr\right)\right]\end{aligned}\tag{13}$$

Along similar lines, the axial pressure gradient may be extracted from Euler's momentum equation, namely,

$$\begin{aligned}\frac{\partial p}{\partial z}=&-\frac{z\kappa^2\lambda_m}{2\pi\beta_{m,0}^2J_1^2\left(\lambda_m\beta_{m,0}\right)}\left(1-e^{-\frac{V}{2\pi}\alpha(1-r)}\right)\\&\times\left\{2\pi\lambda_m\left[J_0^2\left(\lambda_mr\right)+J_1^2\left(\lambda_mr\right)\right]-e^{-\frac{V}{2\pi}\alpha(1-r)}\left[2\pi\lambda_mJ_0^2\left(\lambda_mr\right)-V\alpha J_0\left(\lambda_mr\right)J_1\left(\lambda_mr\right)+2\pi\lambda_mJ_1^2\left(\lambda_mr\right)\right]\right\}\end{aligned}\tag{14}$$

Integrating this expression yields

$$\begin{aligned}\Delta p(r,z)=&-\frac{z^2\kappa^2\lambda_m}{4\pi\beta_{m,0}^2J_1^2\left(\lambda_m\beta_{m,0}\right)}\left(1-e^{-\frac{V}{2\pi}\alpha(1-r)}\right)\\&\times\left\{2\pi\lambda_m\left[J_0^2\left(\lambda_mr\right)+J_1^2\left(\lambda_mr\right)\right]-e^{-\frac{V}{2\pi}\alpha(1-r)}\left[2\pi\lambda_mJ_0^2\left(\lambda_mr\right)-V\alpha J_0\left(\lambda_mr\right)J_1\left(\lambda_mr\right)+2\pi\lambda_mJ_1^2\left(\lambda_mr\right)\right]\right\}\end{aligned}\tag{15}$$

While a unified total solution for the pressure may be obtained for the inviscid solution,[7] the situation is different here because of the approximations incurred during the viscous treatment. At the outset, the pressure differential is no longer exact and so we are unable to meet Euler's integrability criteria. These are discussed in recent work by Saad and Majdalani.[18] Instead, the pressure variation may only be captured along a fixed axis, such as the wall or the centerline. In our case, due to the size of the simulated vortex chambers, the imperfection in the pressure calculation may be deemed immaterial, especially that the contributions from the axial gradient happen to be several orders of magnitude smaller than those from the radial gradient. At the outset, it is reasonable to consider the expression given by Eq. (13) as being representative of the total pressure distribution. The latter is illustrated in Figs. 5c–5d where a large pressure drop is captured near the core. This induced local suction contributes to a negative crossflow that, in turn, assists the fluid traveling in the outer vortex shell to negotiate the 180 degree turn into the inner vortex.

G. Vorticity Characteristics

The vorticity profile can be calculated from

$$\boldsymbol{\omega}=\nabla\times\boldsymbol{u}=-\frac{\partial u_\theta}{\partial z}\boldsymbol{e}_r+\left(\frac{\partial u_r}{\partial z}-\frac{\partial u_z}{\partial r}\right)\boldsymbol{e}_\theta+\left(\frac{\partial u_\theta}{\partial r}+\frac{u_\theta}{r}\right)\boldsymbol{e}_z\tag{16}$$

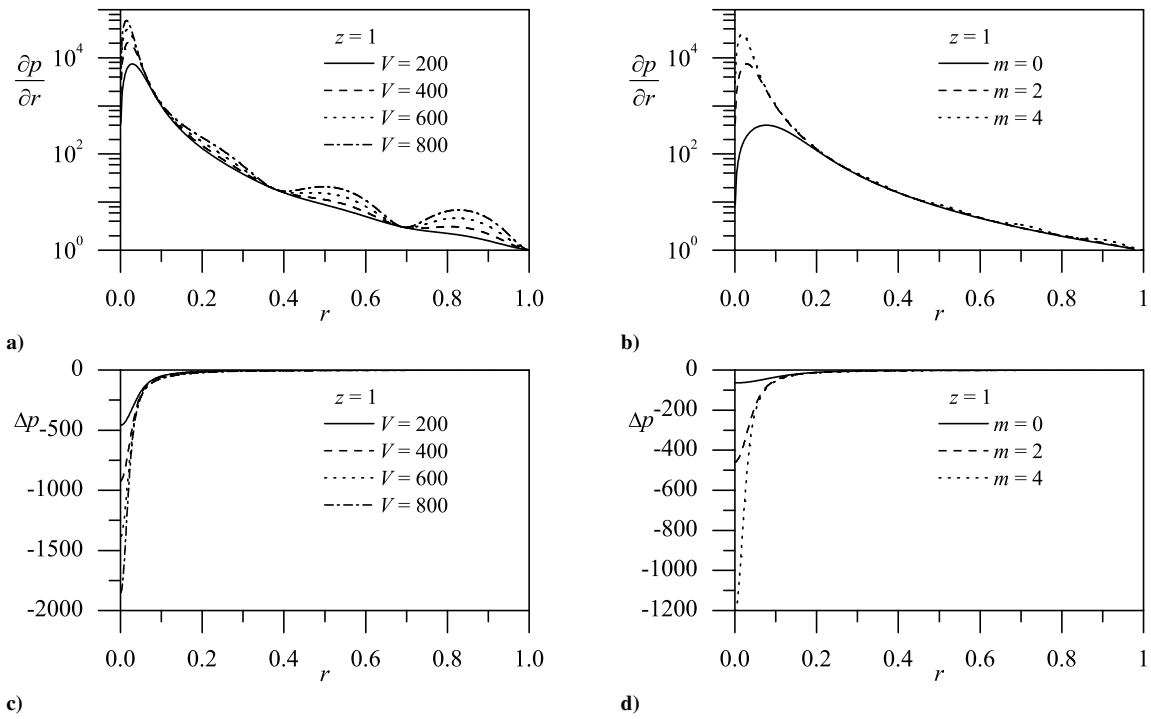

Figure 5. Variation of the radial pressure gradient with respect to a) the vortex Reynolds number with $m = 2$ and b) the flow reversal mode number with $V = 200$. The same variation in the total pressure distribution is showcased in c) and d).

Although this study is directed toward resolving the boundary layers of the Beltramian motion with multiple mantles, it may be worthwhile to compare our findings to those associated with the complex-lamellar multidirectional vortex.[6] As mentioned in Part 1 of this series,[12] the uniqueness of the Beltramian profile lies in its vorticity character. While the complex-lamellar solution engenders only one component of vorticity, namely, $\omega_\theta = 4(m+1)^2\pi^2\kappa rz\sin[(m+1)\pi r^2]$, the axially-dependent tangential velocity here gives rise to a three-dimensional, axisymmetric vorticity field. According to Majdalani,[7] our starting point can be the inviscid vorticity given by

$$\boldsymbol{\omega} = -\frac{rz\kappa^2\lambda_m^2 J_1^2(\lambda_m r)}{\beta_{m,0}^2 J_1(\lambda_m\beta_{m,0})\sqrt{1+\frac{r^2z^2\kappa^2\lambda_m^2 J_1^2(\lambda_m r)}{\beta_{m,0}^2 J_1(\lambda_m\beta_{m,0})}}}\boldsymbol{e}_r + \frac{z\kappa\lambda_m^2 J_1(\lambda_m r)}{\beta_{m,0}J_1(\lambda_m\beta_{m,0})}\boldsymbol{e}_\theta + \frac{rz^2\kappa^2\lambda_m^3 J_0(\lambda_m r)J_1(\lambda_m r)}{\beta_{m,0}^2 J_1(\lambda_m\beta_{m,0})\sqrt{1+\frac{r^2z^2\kappa^2\lambda_m^2 J_1^2(\lambda_m r)}{\beta_{m,0}^2 J_1(\lambda_m\beta_{m,0})}}}\boldsymbol{e}_z \quad (17)$$

It may be easily verified that the expression for $\boldsymbol{\omega}$ leads to a vanishing Lamb vector, $\boldsymbol{\omega}\times\boldsymbol{u} = 0$, thus confirming the onset of Beltramian motion with multiple flow reversals. Thus despite the presence of multiple mantles, we still recover

$$\frac{\boldsymbol{\omega}}{\boldsymbol{u}} = \lambda_m\left[1+\frac{\beta_{m,0}^2 J_1^2(\lambda_m\beta_{m,0})}{\kappa^2\lambda_m^2 r^2 z^2 J_1^2(\lambda_m r)}\right]^{-1/2} \quad (18)$$

The scalar ratio in Eq. (18) confirms the parallelism between the vorticity and the velocity fields throughout the entire chamber. Interestingly, however, this proportionality does not only vary with the spatial location, but also with the flow reversal mode number. For higher modes, the ratio between vorticity and velocity increases substantially. When

frictional forces are accounted for, the corrected form of Eq. (16) turns into

$$\boldsymbol{\omega} = -\frac{rz\kappa^2\lambda_m^2 J_1^2(\lambda_m r)}{\beta_{m,0}^2 J_1(\lambda_m\beta_{m,0})\sqrt{1+\frac{r^2z^2\kappa^2\lambda_m^2 J_1^2(\lambda_m r)}{\beta_{m,0}^2 J_1(\lambda_m\beta_{m,0})}}}\boldsymbol{e}_r + \frac{z\kappa\lambda_m}{\beta_{m,0}J_1(\lambda_m\beta_{m,0})}\left[\frac{V}{2\pi}\alpha J_0(\lambda_m r)\,e^{-\frac{V}{2\pi}\alpha(1-r)} + \lambda_m J_1(\lambda_m r)\left(1-e^{-\frac{V}{2\pi}\alpha(1-r)}\right)\right]\boldsymbol{e}_\theta + \frac{V}{2\pi}\left(2\gamma e^{-\frac{V}{2\pi}\gamma r^2} - r^{-1}e^{-\frac{V}{2\pi}\alpha(1-r)}\right) + \frac{rz^2\kappa^2\lambda_m^3 J_0(\lambda_m r)\,J_1(\lambda_m r)}{\beta_{m,0}^2 J_1(\lambda_m\beta_{m,0})\sqrt{1+\frac{r^2z^2\kappa^2\lambda_m^2 J_1^2(\lambda_m r)}{\beta_{m,0}^2 J_1(\lambda_m\beta_{m,0})}}}\boldsymbol{e}_z \quad (19)$$

Finally, by considering the Pythagorean sum of the vorticity vector, its magnitude may be specified. This effort leads to

$$|\omega| \approx \left\{ r^{-2}\left[\frac{V}{2\pi}\left(2r\gamma e^{-\frac{V}{2\pi}\gamma r^2} - \alpha e^{-\frac{V}{2\pi}\alpha(1-r)}\right) + \frac{r^2z^2\kappa^2\lambda_m^3 J_0(\lambda_m r)\,J_1(\lambda_m r)}{\beta_{m,0}^2 J_1(\lambda_m\beta_{m,0})\sqrt{1+\frac{r^2z^2\kappa^2\lambda_m^2 J_1^2(\lambda_m r)}{\beta_{m,0}^2 J_1(\lambda_m\beta_{m,0})}}}\right] + \frac{V\kappa z^2\lambda_m^2}{4\pi^2\beta_{m,0}^2 J_1^2(\lambda_m\beta_{m,0})}\left[2\pi\lambda_m J_1(\lambda_m r) + e^{-\frac{V}{2\pi}\alpha(1-r)}\left(V\alpha J_0(\lambda_m r) - 2\pi\lambda_m J_1(\lambda_m r)\right)\right]^2\right\}^{1/2} \quad (20)$$

where transcendental terms are discarded. The magnitude of vorticity is displayed in Fig. 6 where its sensitivity with respect to a) z, b) V, and c) m is examined. First, we see in Fig. 6a that the effect of axial excursions is confined to

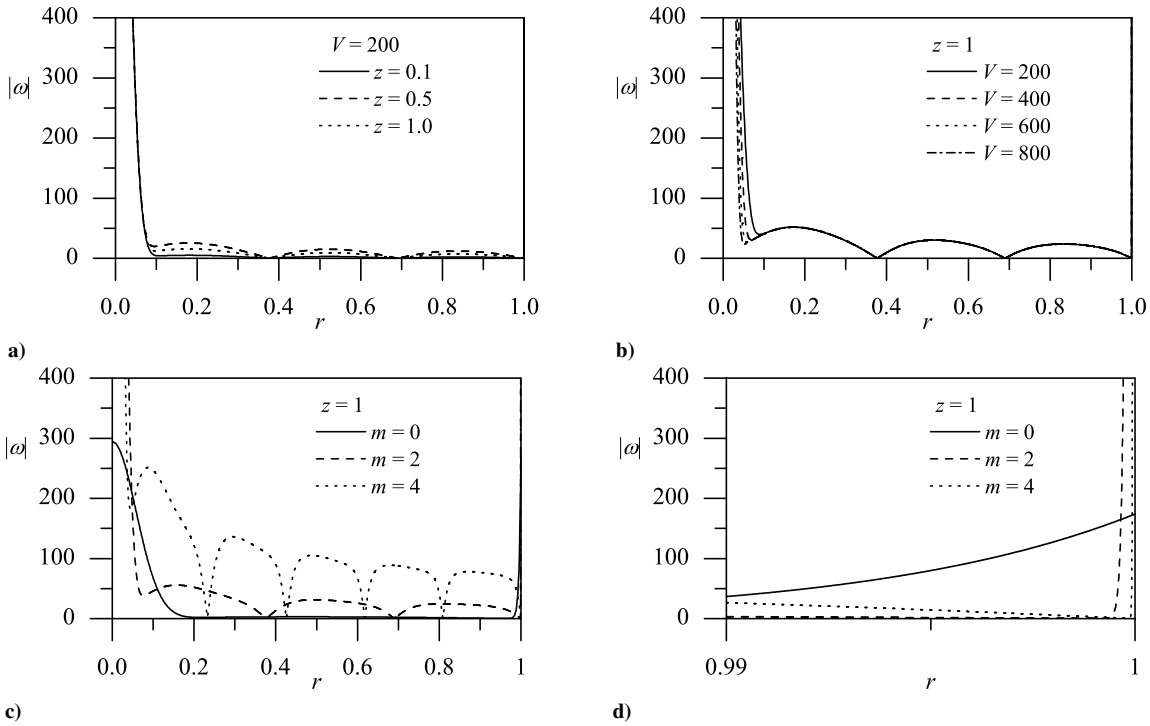

Figure 6. Vorticity distribution with 3 internal mantles showing effects of a) axial variations and b) sequentially increasing V. Parts c) and d) concentrate on the effect of increasing the flow reversal mode number while maintaining $V = 200$.

the bulk, inviscid flow region. Conversely, changes in the vortex Reynolds number, as depicted in Fig. 2b, only seem to influence the forced vortex core region. The most significant result is, perhaps, the strong sensitivity of $\boldsymbol{\omega}$ with respect to m. As it may be inferred from Fig. 6c, increasing the number of mantles is paramount to reducing the radius of the outlet region. The ensuing contraction in cross-sectional area through which the flow may exit gives rise to larger axial velocities in the core region. These in turn induce larger radial velocities by virtue of mass conservation. Pursuant to the velocity amplification, the companion vorticity is forced to increase as well. The steeper vorticity gradients that accompany successive increases in m can be seen to be most pronounced near the mantle locations and fluid boundaries. As shown in Fig. 6d, these lead to progressively sharper curvatures in the boundary layer regions where rapid changes in the velocity must occur.

III. The Nonlinear Beltramian Solution with Multiple Mantles

The analysis of the spatially nonlinear Beltramian solution follows precisely the steps delineated above. The graphical representations of the results are also quite analogous to those just described. In the interest of brevity, only the main expressions will be provided as the reader may reproduce them using, for instance, the corresponding sections that are sufficiently detailed in the treatment of the linear model.

We begin with the multidirectional inviscid streamfunction and velocities that may be given by

$$\psi = \kappa l r \sin\left(\frac{\pi z}{2l}\right) \frac{J_1\left(\lambda_m r\right)}{\beta_{m,0} J_1\left(\lambda_m \beta_{m,0}\right)} \tag{21}$$

and

$$\begin{aligned} \boldsymbol{u} = &-\frac{\pi}{2}\kappa r \cos\left(\frac{\pi z}{2l}\right) \frac{J_1\left(\lambda_m r\right)}{\beta_{m,0} J_1\left(\lambda_m \beta_{m,0}\right)} \boldsymbol{e}_r \\ &+ r^{-1} \sqrt{1 + \frac{\kappa^2}{\beta_{m,0}^2 J_1^2\left(\lambda_m \beta_{m,0}\right)} \left(\lambda_m^2 l^2 + \frac{1}{4}\pi^2\right) r^2 \sin^2\left(\frac{\pi z}{2l}\right) J_1^2\left(\lambda_m r\right)}\, \boldsymbol{e}_\theta \\ &+ \kappa l \lambda_m \sin\left(\frac{\pi z}{2l}\right) \frac{J_0\left(\lambda_m r\right)}{\beta_{m,0} J_1\left(\lambda_m \beta_{m,0}\right)} \boldsymbol{e}_z \end{aligned} \tag{22}$$

where, as usual, $\kappa = Q_i/(2\pi l)$ and $\lambda_m = \{3.83171, 7.01559, 10.1735, 13.3237, \cdots\}$.

Next, by adapting the viscous treatment by Batterson and Majdalani[13] for the bidirectional case, we can directly extrapolate the multidirectional flow analog. We find

$$\begin{aligned} \boldsymbol{u} = &-\frac{\pi\kappa}{2\beta_{m,0} J_1\left(\lambda_m \beta_{m,0}\right)} \cos\left(\frac{\pi z}{2l}\right) J_1\left(\lambda_m r\right) \left(1 - e^{-\frac{V}{2\pi}\alpha(1-r)}\right) \boldsymbol{e}_r \\ &+ r^{-1} \left\{ \left[1 + \frac{\kappa^2}{\beta_{m,0}^2 J_1^2\left(\lambda_m \beta_{m,0}\right)} \left(\lambda_m^2 l^2 + \tfrac{1}{4}\pi^2\right) r^2 \sin^2\left(\frac{\pi z}{2l}\right) J_1^2\left(\lambda_m r\right) \right]^{1/2} - e^{-\frac{V}{2\pi}\gamma r^2} - e^{-\frac{V}{2\pi}\alpha(1-r)} \right\} \boldsymbol{e}_\theta \\ &+ \frac{\lambda_m \kappa l}{\beta_{m,0} J_1\left(\lambda_m \beta_{m,0}\right)} \sin\left(\frac{\pi z}{2l}\right) J_0\left(\lambda_m r\right) \left(1 - e^{-\frac{V}{2\pi}\alpha(1-r)}\right) \boldsymbol{e}_z \end{aligned} \tag{23}$$

where, as before, $\alpha = \lambda_m \left(\frac{1}{8}\lambda_m^2 - 1\right)/[2\beta_{m,0} J_1(\lambda_m \beta_{m,0})]$ and $\gamma = \lambda_m/[4\beta_{m,0} J_1(\lambda_m \beta_{m,0})]$. From the velocity, the boundary layers may be ascertained. For the inner core layer, we obtain

$$\delta_i \approx \sqrt{\frac{2\beta_{m,0} J_1\left(\lambda_m \beta_{m,0}\right)}{\kappa^2 \lambda_m \left(\pi^2 + 4l^2 \lambda_m^2\right)} \csc^2\left(\frac{\pi z}{2l}\right) \left(-V + \sqrt{V^2 + 4\pi^2 \kappa^2 \left(\pi^2 + 4l^2 \lambda_m^2\right)\left[1 - \cos\left(\pi z/l\right)\right] \ln\left(100\right)}\right)} \tag{24}$$

and

$$\delta_w = 1 - r \approx \frac{2\pi}{V\alpha} \ln\left(100\right) \tag{25}$$

Only slight differences in the boundary layer thickness between the linear and nonlinear solutions may be reported as one may infer from Table 4. The particular properties that accompany successive increases in the mode number, previously illustrated in Table 3, apply equally well.

Table 4. Prandtl's inner core and sidewall boundary layer thicknesses for the nonlinear Beltramian model at different positions and vortex Reynolds numbers. Here $\kappa = 0.103$, $m = 0$ and $l = 1$

	Inner boundary layer, δ_i					Sidewall boundary layer, δ_w				
z	$V = 200$	$V = 400$	$V = 600$	$V = 800$	$V = 1000$	$V = 200$	$V = 400$	$V = 600$	$V = 800$	$V = 1000$
0.0	0.2218	0.1569	0.1281	0.1109	0.0992	0.0295	0.0147	0.0098	0.0074	0.0059
0.25	0.2218	0.1569	0.1281	0.1109	0.0992	0.0295	0.0147	0.0098	0.0074	0.0059
0.5	0.2218	0.1568	0.1281	0.1109	0.0992	0.0295	0.0147	0.0098	0.0074	0.0059
0.75	0.2217	0.1568	0.1281	0.1109	0.0992	0.0294	0.0147	0.0098	0.0074	0.0059
1.0	0.2217	0.1568	0.1281	0.1109	0.0992	0.0294	0.0147	0.0098	0.0074	0.0059

The pressure distribution stems from Euler's equation. For the radial pressure gradient, we get

$$\frac{\partial p}{\partial r} \approx \frac{1}{r^3}\left(e^{-\frac{V}{\pi}\alpha(1-r)} + e^{-\frac{V}{\pi}\gamma r^2} - 2e^{-\frac{V}{2\pi}\alpha(1-r)} + 2e^{-\frac{V}{2\pi}\gamma r^2}\right) \tag{26}$$

and, for the pressure differential $\Delta p = p - p_0$ referenced to the headwall corner, $p_0 = p(1,0)$, we find

$$\begin{aligned}\Delta p\,(r,z) = &-\frac{1}{2} - \frac{V}{2\pi}\alpha - \frac{1}{2r^2} + \frac{\pi^2 + \pi\alpha V - \alpha^2 V^2 \mathrm{Ei}\left(\frac{V}{\pi}\alpha\right) e^{-\frac{V}{\pi}\alpha}}{2\pi^2} \\ &- \frac{\pi\left(\pi + V\alpha r\right) e^{-\frac{V}{\pi}\alpha(1-r)} - r^2\alpha^2 V^2 \mathrm{Ei}\left(\frac{V}{\pi}\alpha r\right) e^{-\frac{V}{\pi}\alpha}}{2\pi^2 r^2} \\ &+ \frac{1}{r^2}\left(e^{-\frac{V}{2\pi}\gamma r^2} - \frac{1}{2}e^{-\frac{V}{\pi}\gamma r^2}\right) + \frac{\pi}{2\pi}\left(e^{-\frac{V}{\pi}\gamma} - 2e^{-\frac{V}{2\pi}\gamma}\right) + \frac{V\gamma}{2\pi}\left[\mathrm{Ei}\left(-\frac{V}{\pi}\gamma\right) - \mathrm{Ei}\left(-\frac{V}{\pi}\gamma r^2\right)\right] \\ &+ \frac{V\gamma}{2\pi}\left[\mathrm{Ei}\left(-\frac{V}{2\pi}\gamma r^2\right) - \mathrm{Ei}\left(-\frac{V}{2\pi}\gamma\right)\right] + \frac{\alpha^2 V^2}{4\pi^2}\mathrm{Ei}\left(\frac{V}{2\pi}\alpha\right) e^{-\frac{V}{2\pi}\alpha} \\ &+ \frac{2\pi\left(2\pi + V\alpha r\right) e^{-\frac{V}{2\pi}\alpha(1-r)} - r^2\alpha^2 V^2 \mathrm{Ei}\left(\frac{V}{2\pi}\alpha r\right) e^{-\frac{V}{2\pi}\alpha}}{4r^2\pi^2}\end{aligned} \tag{27}$$

In the present case, the pressure and its radial gradient do not spatially undulate as noticeably as their linear Beltramian counterparts at higher values of m. This may be due to the markedly diminished dependence of Eqs. (26–27) on z.

Finally, the vorticity field may be deduced from Eq. (23) which returns

$$\begin{aligned}\boldsymbol{\omega} = &-\frac{\pi r\kappa^2\left(\frac{\pi^2}{4} + l^2{\lambda_m}^2\right){J_1}^2\left(\lambda_m r\right)}{4l\beta_{m,0}^2 J_1\left(\lambda_m\beta_{m,0}\right)\sqrt{1 + \frac{r^2\kappa^2\left(\frac{\pi^2}{4} + l^2{\lambda_m}^2\right)}{\beta_{m,0}^2 {J_1}\left(\lambda_m\beta_{m,0}\right)}\sin^2\left(\frac{\pi}{l}z\right){J_1}^2\left(\lambda_m r\right)}}\sin\left(\frac{\pi}{l}z\right)\boldsymbol{e}_r \\ &+ \frac{\kappa}{l\beta_{m,0}J_1\left(\lambda_m\beta_{m,0}\right)}\sin\left(\frac{\pi}{2l}z\right)\left\{\frac{Vl^2\alpha\lambda_m}{2\pi}J_0\left(\lambda_m r\right)e^{-\frac{V}{2\pi}\alpha(1-r)} + \left(\frac{\pi^2}{4} + l^2{\lambda_m}^2\right)J_1\left(\lambda_m r\right)\left(1 - e^{-\frac{V}{2\pi}\alpha(1-r)}\right)\right\}\boldsymbol{e}_\theta \\ &+ \left\{\frac{V}{2\pi}\left(2\gamma e^{-\frac{V}{2\pi}\gamma r^2} - r^{-1}\alpha e^{-\frac{V}{2\pi}\alpha(1-r)}\right) + \frac{r\kappa^2\lambda_m J_0\left(\lambda_m r\right)J_1\left(\lambda_m r\right)\left(\frac{\pi^2}{4} + l^2{\lambda_m}^2\right)\left[1 - \cos\left(\frac{\pi}{l}z\right)\right]}{4\beta_{m,0}^2 J_1^2\left(\lambda_m\beta_{m,0}\right)\sqrt{1 + \frac{r^2\kappa^2\left(\frac{\pi^2}{4} + l^2{\lambda_m}^2\right)}{\beta_{m,0}^2 {J_1}\left(\lambda_m\beta_{m,0}\right)}\sin^2\left(\frac{\pi}{l}z\right){J_1}^2\left(\lambda_m r\right)}}\right\}\boldsymbol{e}_z\end{aligned} \tag{28}$$

with the net magnitude of

$$|\omega| = \left\{ \frac{\kappa^2\left(-2e^{-\frac{V}{2\pi}\alpha(1-r)}Vl^2\alpha\lambda_m J_0\left(\lambda_m r\right) - \left(1-e^{-\frac{V}{2\pi}\alpha(1-r)}\right)\pi\left(\pi^2+4l^2{\lambda_m}^2\right)J_1\left(\lambda_m r\right)\right)^2}{16l^2\pi^2\beta_{m,0}^2{J_1}^2\left(\lambda_m\beta_{m,0}\right)}\sin^2\left(\frac{\pi z}{2l}\right) \right.$$

$$+ r^{-2}\left[\frac{V}{\pi}\gamma r e^{-\frac{V}{2\pi}\gamma r^2} - \frac{V}{2\pi}\alpha e^{-\frac{V}{2\pi}\alpha(1-r)}\right.$$

$$\left. + \frac{r\kappa^2\left(\pi^2+4l^2{\lambda_m}^2\right)\sin^2\left(\frac{\pi z}{2l}\right)J_1\left(\lambda_m r\right)\left[r\lambda_m J_0\left(\lambda_m r\right)+2J_1\left(\lambda_m r\right)-r\lambda_m J_2\left(\lambda_m r\right)\right]}{4\beta_{m,0}^2 J_1^2\left(\lambda_m\beta_{m,0}\right)\sqrt{4+\frac{r^2\kappa^2z^2\left(\pi^2+4l^2{\lambda_m}^2\right){J_1}^2(\lambda_m r)}{\beta_{m,0}^2{J_1}^2\left(\lambda_m\beta_{m,0}\right)}\sin^2\left(\frac{\pi z}{2l}\right)}}\right]^2$$

$$\left. + \frac{\pi^2r^2\kappa^4\left(\pi^2+4l^2{\lambda_m}^2\right)^2\sin^2\left(\frac{\pi z}{l}\right)J_1^4\left(\lambda_m r\right)}{64l^2\beta_{m,0}^2{J_1}^2\left(\lambda_m\beta_{m,0}\right)\left[4\beta_{m,0}^2{J_1}^2\left(\lambda_m\beta_{m,0}\right)+r^2\kappa^2\left(\pi^2+4l^2{\lambda_m}^2\right)J_1^2\left(\lambda_m r\right)\sin^2\left(\frac{\pi z}{2l}\right)\right]}\right\}^{1/2} \tag{29}$$

IV. Results and Discussion

In this section, we compare our results to the multidirectional form of the sinusoidal profile discussed originally by Vyas, Majdalani and Chiaverini.[10] By augmenting its formulation with three-dimensional viscous corrections,[14] we arrive at

$$\boldsymbol{u} = -\frac{\kappa}{r}\sin[(m+1)\pi r^2]\left[1-e^{-\frac{V}{4}(m+1)\alpha(1-r^2)}\right]\boldsymbol{e}_r$$
$$+ r^{-1}\left[1-e^{-\frac{V}{4}(m+1)r^2}-e^{-\frac{V}{4}(m+1)\alpha(1-r^2)}\right]\boldsymbol{e}_\theta$$
$$+ 2(m+1)\pi\kappa z\cos[(m+1)\pi r^2]\left[1-e^{-\frac{V}{4}(m+1)\alpha(1-r^2)}\right]\boldsymbol{e}_z \tag{30}$$

where $\alpha = \frac{1}{6}(m+1)^2\pi^2 - 1$ may be associated with the complex-lamellar solution.

In Fig. 7, vector diagrams of the Beltramian models are displayed along with the complex-lamellar analog. These graphs show that a higher centerline velocity persists farther downstream in the nonlinear profile than in any other

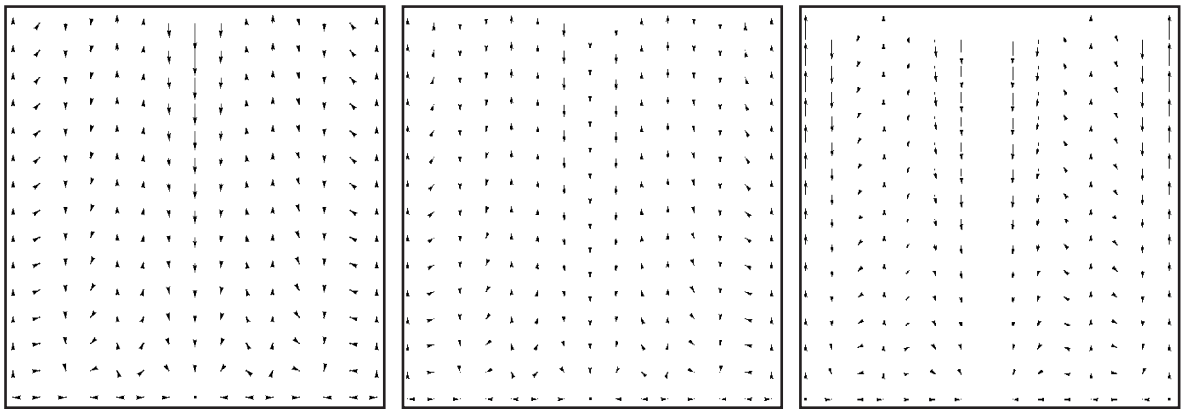

a) Linear Beltramian **b)** Nonlinear Beltramian **c)** Complex Lamellar

Figure 7. Vector plots of a) linear Beltramian, b) nonlinear Beltramian, and c) complex-lamellar models. Here $l = 2$.

model. The vector directions also suggest, in the nonlinear solution, a headwall-skewed crossflow along the mantle surface. This leads to higher crossflow velocities near the headwall, and reduced spillage near the endwall. Such behavior is quite advantageous as it is more desirable to limit, as much as possible, any mass transport near $z = l$ from the outer vortex into the inner core. In the VCCWC configuration, the outer vortex near $z = l$ contains a freshly injected oxidizer that has not yet reacted with the fuel. The nonlinear Beltramian motion seems to be optimal for fuel injection near the headwall where crossing of the outer 'oxidizer' fluid is maximized, and leakage near the nozzle attachment section is minimized. For the reader's convenience, a comparison of the complex-lamellar and linear Beltramian models is furnished in Table 5. Therein, it may be remarked that the viscous character in both linear and nonlinear Beltramian approximations is identical. This marks the differences in the inviscid solutions as the delimiting characteristics for each flowfield. These seem to infuse the boundary layer profile during matching, but not to a significant degree.

Table 5. Comparison between the complex-lamellar,[19] linear, and nonlinear Beltramian models[7]

Complex Lamellar	$\alpha = \frac{1}{6}(m+1)^2\pi^2 - 1$
u_r	$-\frac{\kappa}{r}\sin\left[(m+1)\pi r^2\right]\left[1 - e^{-\frac{V}{4}(m+1)\alpha(1-r^2)}\right]$
u_θ	$\frac{1}{r}\left[1 - e^{-\frac{V}{4}(m+1)r^2} - e^{-\frac{V}{4}(m+1)\alpha\left(1-r^2\right)}\right]$
u_z	$2(m+1)\pi\kappa z\cos\left[(m+1)\pi r^2\right]\left[1 - e^{-\frac{V}{4}(m+1)\alpha(1-r^2)}\right]$
δ_i, δ_w	$\sqrt{\frac{4\ln 100}{V(m+1)}}$; $\delta_w = 1 - \sqrt{1 - \frac{4\ln 100}{V(m+1)\alpha}}$
Linear Beltramian	$\alpha = \frac{\lambda_m}{2\beta_{m,0}J_1\left(\lambda_m\beta_{m,0}\right)}\left(\frac{1}{8}\lambda_m^2 - 1\right)$ $\quad \gamma = \frac{\lambda_m}{4\beta_{m,0}J_1(\lambda_m\beta_{m,0})}$
u_r	$-\frac{\kappa J_1(\lambda_m r)}{\beta_{m,0}J_1\left(\lambda_m\beta_{m,0}\right)}\left[1 - e^{-\frac{V}{2\pi}\alpha(1-r)}\right]$
u_θ	$\frac{1}{r}\left[\left(1 + \frac{\lambda_m^2\kappa^2r^2z^2J_1^2(\lambda_m r)}{\beta_{m,0}^2J_1^2\left(\lambda_m\beta_{m,0}\right)}\right)^{1/2} - e^{-\frac{V}{2\pi}\gamma r^2} - e^{-\frac{V}{2\pi}\alpha(1-r)}\right]$
u_z	$\frac{\lambda_m\kappa z J_0(\lambda_m r)}{\beta_{m,0}J_1\left(\lambda_m\beta_{m,0}\right)}\left[1 - e^{-\frac{V}{2\pi}\alpha(1-r)}\right]$
δ_i, δ_w	$\sqrt{\frac{\beta_{m,0}J_1\left(\lambda_m\beta_{m,0}\right)}{2\pi z^2\kappa^2\lambda_m^3}\left(-V + \sqrt{V^2 + 32\pi^2z^2\kappa^2\lambda_m^2\ln(100)}\right)}$; $\delta_w \approx \frac{2\pi}{V\alpha}\ln(100)$
Nonlinear Beltramian	$\alpha = \frac{\lambda_m}{2\beta_{m,0}J_1\left(\lambda_m\beta_{m,0}\right)}\left(\frac{1}{8}\lambda_m^2 - 1\right)$ $\quad \gamma = \frac{\lambda_m}{4\beta_{m,0}J_1(\lambda_m\beta_{m,0})}$
u_r	$-\frac{\pi\kappa}{2\beta_{m,0}J_1\left(\lambda_m\beta_{m,0}\right)}\cos\left(\frac{\pi z}{2l}\right)J_1\left(\lambda_m r\right)\left(1 - e^{-\frac{V}{2\pi}\alpha(1-r)}\right)$
u_θ	$r^{-1}\left\{\left[1 + \frac{\kappa^2}{\beta_{m,0}^2J_1^2\left(\lambda_m\beta_{m,0}\right)}\left(\lambda_m^2l^2 + \frac{1}{4}\pi^2\right)r^2\sin^2\left(\frac{\pi z}{2l}\right)J_1^2\left(\lambda_m r\right)\right]^{1/2} - e^{-\frac{V}{2\pi}\gamma r^2} - e^{-\frac{V}{2\pi}\alpha(1-r)}\right\}$
u_z	$\frac{\lambda_m\kappa l}{\beta_{m,0}J_1\left(\lambda_m\beta_{m,0}\right)}\sin\left(\frac{\pi z}{2l}\right)J_0\left(\lambda_m r\right)\left(1 - e^{-\frac{V}{2\pi}\alpha(1-r)}\right)$
δ_i, δ_w	$\sqrt{\frac{2\beta_{m,0}J_1\left(\lambda_m\beta_{m,0}\right)}{\kappa^2\lambda_m\left(\pi^2+4l^2\lambda_m^2\right)}\csc^2\left(\frac{\pi z}{2l}\right)\left(-V + \sqrt{V^2 + 4\pi^2\kappa^2\left(\pi^2 + 4l^2\lambda_m^2\right)[1 - \cos(\pi z/l)]\ln(100)}\right)}$; $\delta_w \approx \frac{2\pi}{V\alpha}\ln(100)$

Table 6. Comparison of experimental and computational mantle locations with the complex-lamellar (CL) and Beltramian (BT) models

			Experimental			Computational		
n	$\beta_{2,n}^{(\mathrm{CL})}$	$\beta_{2,n}^{(\mathrm{BT})}$	$\beta_{2,n}^{(\mathrm{EXP})}$	$\lvert\beta_{2,n}^{(\mathrm{CL})} - \beta_{2,n}^{(\mathrm{EXP})}\rvert$	$\lvert\beta_{2,n}^{(\mathrm{BT})} - \beta_{2,n}^{(\mathrm{EXP})}\rvert$	$\beta_{2,n}^{(\mathrm{CFD})}$	$\lvert\beta_{2,n}^{(\mathrm{CL})} - \beta_{2,n}^{(\mathrm{CFD})}\rvert$	$\lvert\beta_{2,n}^{(\mathrm{BT})} - \beta_{2,n}^{(\mathrm{CFD})}\rvert$
0	0.408	0.236	0.296	0.112	0.060	0.305	0.103	0.069
1	0.707	0.543	0.594	0.113	0.051	0.385	0.322	0.158
2	0.913	0.851	0.803	0.110	0.048	0.787	0.126	0.064

A. Experimental Validation

Table 6 compares the experimental and numerical findings of Anderson and co-workers[8,9,20] to ours. This comparison is carried out under the premise that 3 internal mantles are developed (i.e., $m = 2$). At this point in time, it appears that the set of operating conditions that triggers the onset of multiple mantles remains a subject of investigation.

Based on the available empirical measurements, it is clear that the Beltramian model outperforms other models, including numerical simulations, in predicting the location of the internal mantles. The empirical results in Table 6 are taken from Anderson, Rom and coworkers.[8,9,20] These seem to suggest that, in the presence of 3 mantles, the original complex-lamellar model is less precise than the Beltramian solution in capturing the flow reversal radial spacing. Having no access to the 2009 Beltramian formulation, Rom, Anderson and Chiaverini[9] note that the complex-lamellar model with 4 mantles matches quite remarkably their experimental and computational predictions. However, based on the present investigation, it does not appear that four mantles are likely to form without moving the primary injection plane to the headwall. Realizing that Anderson's injection of the outer fluid occurs near the endwall, the comparison with 4 mantles is possibly amiss. The confusion may be attributed to inevitable bias in the experimental measurements in the close vicinity of the sidewall. Instead, it is our belief that the 4-mantle case reported by Anderson and coworkers actually corresponds to a 3-mantle configuration with $m = 2$. As it may be inferred from Table 6, the Beltramian approximation seems to be the most trustworthy as it concurs reasonably well with both experimental and computation results. It is therefore recommended for use in modeling multidirectional vortex behavior.

Turning our attention to the actual velocity and pressure distributions associated with the three analytical models, it may be seen in Figure 8 that a substantial increase occurs in the axial and tangential Beltramian speeds over their complex-lamellar counterparts in a 3-mantle configuration. This comparison is carried out using $V = 200$, $m = 2$, and $z = l = 1$, except for the radial plot displayed in Fig. 8c where u_r is taken halfway in the chamber at $z/l = \frac{1}{2}$. Apart from the graph associated with u_r, the linear and nonlinear Beltramian models seem to coincide. At the point of comparison, their tangential, axial, and pressure distributions seem indiscernible.

In relation to the sinusoidal model, the larger tangential velocity associated with the Beltramian model near the core translates into a much steeper vacuum pressure that can be observed in Fig. 8d. As for the mantle spacing depicted in Fig. 8b, it can be seen that spacing between Beltramian mantles remains nearly constant at higher modes in contrast to the r^2 dependence displayed by the complex-lamellar solution. The latter leads to a decreased spacing near the sidewall.

By comparison to the Beltramian solutions that are spatially influenced by increased values of m, the inviscid character of the complex-lamellar u_θ limits its sensitivity on m to the viscous regions. The reason may be attributed to the mode number only affecting the relationship between the axial and radial velocities that remain linked through continuity. As such, the axially independent u_θ remains somewhat immune to variations in m. In contrast, the Beltramian tangential velocity only recovers the complex-lamellar behavior at the zeroes of $J_1(\lambda_m r)$.

As showcased in Fig. 8, both linear and nonlinear Beltramian solutions become virtually identical in their tangential and axial components when evaluated in the exit plane. Because the nonlinear Beltramian u_r vanishes in the exit plane, the results in Fig. 8c are quantified at the chamber midpoint. This characteristic feature of the nonlinear solution is, perhaps, the most consistent with the ideal inlet condition that implies a purely tangential inflow.

B. Crossflow Velocity

The vector plots displayed in Fig. 7 show that the multidirectional solutions exhibit both positive and negative crossflow velocities along alternating mantle locations. For physically viable solutions to exist, the overall crossflow velocity must be negative. This requirement is essential to ensure that the overall movement of the fluid is directed

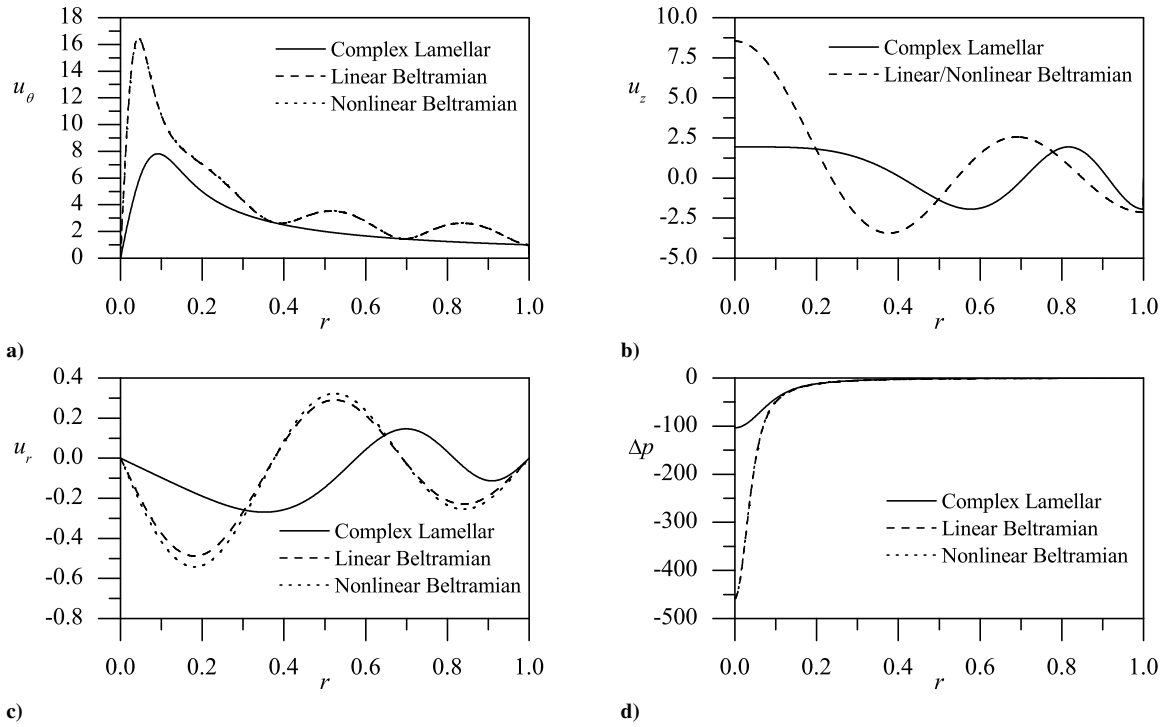

Figure 8. Side-by-side comparison for the three components of velocity a) u_θ, b) u_z, c) u_r and d) the pressure difference from the head-end corner using various helical models. We take $m = 2$, $z = l = 1$ and $V = 200$ except for the radial velocity which we evaluate at $z = \frac{1}{2}l$.

toward the core and, subsequently, toward the open section at the endwall. The orientation of the crossflow can be ascertained by averaging the radial velocity over the domain to the extent of getting

Beltramian (both linear and nonlinear):

$$u_r^{avg} = \frac{1}{V}\iiint_V u_r \, r \, \mathrm{d}r \, \mathrm{d}z \, \mathrm{d}\theta = -\frac{\kappa\lambda_m \Phi\left[\left(\frac{3}{2}\right), \left(2, \frac{5}{2}\right), -\frac{\lambda_m^2}{4}\right]}{3\beta_{m,0} J_1\left(\lambda_m \beta_{m,0}\right)} \tag{31}$$

Complex Lamellar:

$$u_r^{avg} = -\kappa\sqrt{\frac{2}{m+1}}\,\mathrm{S}\left(\sqrt{2(m+1)}\right) \tag{32}$$

where Φ is the general hypergeometric function and S is the Fresnel sine integral.

In Fig. 9, the average crossflow velocity is calculated and posted at increasing flow reversal mode numbers, $m = 0, 1, 2, \ldots, 11$. In this effort, it can be seen that the complex lamellar crossflow maintains a negative average for all mode numbers while the Beltramian average returns a negative outcome for even modes only. This behavior confirms that our solution is only valid for an odd number of mantles and therefore consistent with aft end injection. The non-alternating sign of the average crossflow velocity associated with the complex-lamellar solution may also explain the confusion that can befall its users, specifically those who may inadvertently consider spurious configurations with an even number of mantles. Interestingly, the crossflow velocities in all cases approach a very small value asymptotically with m. Then as the Beltramian odd modes approach from the top, the corresponding even modes approach from the bottom. This alternating nature and rate of convergence is consistent with the behavior of the hypergeometric function that appears in the numerator of Eq. (31). As an aside, the asymptotic convergence to zero can be easily verified for the complex-lamellar solution by taking the limit of Eq. (32) as $m \to \infty$. However, the same limit appears to be analytically intractable for the Beltramian crossflow equation.

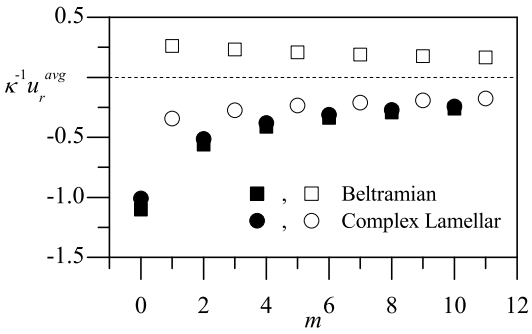

Figure 9. Average crossflow velocities at several successive mode numbers. Even and odd mode numbers are designated by full and hollow symbols, respectively.

C. Maximum Velocity and Forced Vortex Character

It may be useful to recall that the forced vortex thickness, δ_c, is defined as the radial distance from the centerline to the point of $(u_\theta)_{\max}$. In reviewing both linear and nonlinear Beltramian solutions, a common approximation may be realized for the case of multiple mantles. In fact, both models seem to exhibit a forced vortex thickness that may be estimated from

$$\delta_c \approx 2\sqrt{\frac{\pi\beta_{m,0}J_1(\beta_{m,0}\lambda_m)}{\lambda_m V}\left[-1-2\,\mathrm{pln}\left(-1,-\frac{1}{2\sqrt{e}}\right)\right]} \tag{33}$$

In like manner, the peak tangential velocity may be expressed as

$$(u_\theta)_{\max} \approx \frac{1-e^{\frac{1}{2}+\mathrm{pln}\left(-1,-\frac{1}{2\sqrt{e}}\right)}}{2\sqrt{\pi\beta_{m,0}J_1(\beta_{m,0}\lambda_m)\left[-1-2\,\mathrm{pln}\left(-1,-\frac{1}{2\sqrt{e}}\right)\right]}}\sqrt{\lambda_m V} \tag{34}$$

D. Vorticity Magnitudes

Figure 10 compares constant vorticity lines associated with the three models under discussion. Only the magnitude of vorticity is displayed in these graphs to the extent that no negative values appear. In reality, vorticity can alternate signs inversely with the radial velocity. As it may be anticipated, the Beltramian flows are generally accompanied by steeper velocities and, as such, larger vorticity magnitudes, with the most intense of which being found in the nonlinear case. Overall, we find vorticity amplification as we approach the centerline in both Beltramian solutions. In contrast, the complex-lamellar vorticity is seen to increase near the sidewall. In the same vein, higher vorticity may be detected deep in the core region of the Beltramian model, unlike its counterpart. When all three vorticity fields are compared, the nonlinear solution may be seen to induce the most intense and widespread vorticity distribution. We speculate that multiple alternating vorticity fields, such as those associated with the nonlinear Beltramian motion, are more likely to trigger turbulence and flow instability than any uni- or bi-directional flow motion.

V. Conclusions

This study constitutes the third and final installment of a paper series that is focused on the Beltramian vortex motion that arises in the context of confined cyclonic chambers. In Parts 1 and 2, [12,13] we have described the asymptotic analysis leading to viscous approximations for the spatially linear and nonlinear formulations. In the process, we have improved the existing inviscid solutions by removing their centerline singularities and permitting them to satisfy the no-slip condition at the sidewall.

Part 3 has focused on the multidirectional motion of a fluid that undergoes two or more flow reversals before exiting the chamber. This multilayered flow configuration is predicted mathematically and confirmed both experimentally and numerically. In the case of the Beltramian motions, their multidirectional character is found to be strongly dependent

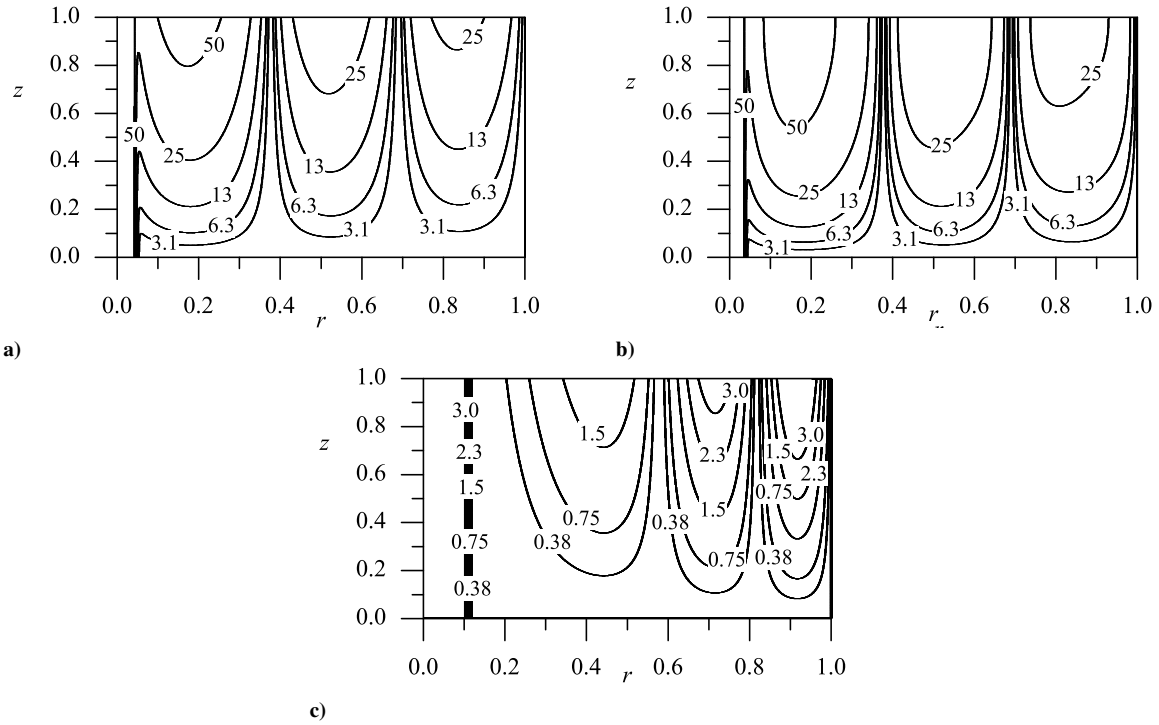

Figure 10. Isovorticity lines corresponding to a) linear, b) nonlinear Beltramian, and c) complex-lamellar vortex models. [19]

on the mode number, m, both in their inviscid and viscous flow segments. The effect of the mode number on the bulk fluid translates into multiple vortex tubes of alternating axial velocity. The companion crossflow alternates directions to keep up with the axial motion by way of continuity. For physically plausible flow scenarios, an odd number of mantles is required, and the corresponding average crossflow is confirmed to remain indeed negative, and therefore inward pointing, for all even mode numbers. The behavior of the nonlinear Beltramian solution is found to be most intriguing as it is accompanied by intense velocity and vorticity, increased mixing at the headwall, and reduced leakage at the endwall. This decrease in spillage near the outlet section is highly desirable in propulsive applications where it is essential to inhibit oxidizer leakage. Conversely, the increased crossflow near the headwall is advantageous as it leads to improved mixing with the injected fuel. A larger crossflow velocity near the headwall also translates into increased residence time.

In what concerns the boundary layers, we find the sidewall layer of the complex-lamellar model to embody an $(m + 1)^{-3}$ dependence on the number of mantles. A similar dependence is seen to underlie both Beltramian models. This behavior results in very thin sidewall layers for $m \geq 2$. On the one hand, such minuscule regions can in fact be discounted in the majority of flow calculations. On the other hand, the forced vortex that forms at the centerline is seen to exhibit a depreciation in core thickness but a magnification in the maximum velocity as the flow reversal mode number is increased. As to be expected, the ensuing velocity amplification propagates into other flow properties such as the pressure and vorticity, thus pushing them to higher peak values with successive increases in m.

Acknowledgments

This project was completed with support from the National Science Foundation through Grant No. CMMI-0928762, Dr. Eduardo A. Misawa, Program Director.

References

[1]Çengel, Y. A., *Introduction to Thermodynamics and Heat Transfer*, McGraw-Hill, New York, 1996.
[2]Çengel, Y. A., *Heat Transfer: A Practical Approach*, McGraw-Hill, New York, 1998.

[3]Gloyer, P. W., Knuth, W. H., and Goodman, J., "Overview of Initial Research into the Effects of Strong Vortex Flow on Hybrid Rocket Combustion and Performance," *CSTAR Fifth Annual Symposium*, Paper N96-16953, Tullahoma, Tennessee, Jan. 1993.

[4]Knuth, W., Chiaverini, M., Sauer, J., and Gramer, D., "Solid-Fuel Regression Rate Behavior of Vortex Hybrid Rocket Engines," *Journal of Propulsion and Power*, Vol. 18, No. 3, 2002, pp. 600–609. doi:10.2514/2.5974.

[5]Chiaverini, M., Malecki, M., Sauer, J., Knuth, W., and Majdalani, J., "Vortex Thrust Chamber Testing and Analysis for O2-H2 Propulsion Applications," *39th AIAA/ASME/SAE/ASEE Joint Propulsion Conference and Exhibit*, AIAA Paper 2003-4473, Huntsville, Alabama, July 2003.

[6]Vyas, A., and Majdalani, J., "Exact Solution of the Bidirectional Vortex," *AIAA Journal*, Vol. 44, No. 10, 2006, pp. 2208. doi:10.2514/1.14872.

[7]Majdalani, J., "Exact Eulerian Solutions of the Cylindrical Bidirectional Vortex," *45th AIAA/ASME/SAE/ASEE Joint Propulsion Conference and Exhibit*, AIAA Paper 2009-5307, Denver, Colorado, Aug. 2009.

[8]Anderson, M., Valenzuela, R., Rom, C., Bonazza, R., and Chiaverini, M., "Vortex Chamber Flow Field Characterization for Gelled Propellant Combustor Applications," *39th AIAA/ASME/SAE/ASEE Joint Propulsion Conference and Exhibit*, AIAA Paper 2003-4474, Huntsville, Alabama, July 2003.

[9]Rom, C. J., Anderson, M. H., and Chiaverini, M. J., "Cold Flow Analysis of a Vortex Chamber Engine for Gelled Propellant Combustor Applications," *40th AIAA/ASME/SAE/ASEE Joint Propulsion Conference and Exhibit*, AIAA Paper 2004-3359, 2004.

[10]Vyas, A., Majdalani, J., and Chiaverini, M., "The Bidirectional Vortex. Part 3: Multiple Solutions," *39th AIAA/ASME/SAE/ASEE Joint Propulsion Conference and Exhibit*, AIAA Paper 2003-5054, Huntsville, Alabama, July 2003.

[11]Matveev, I., Matveeva, S., and Serbin, S., "Design and Preliminary Test Results of the Plasma Assisted Tornado Combustor," *43rd AIAA Joint Propulsion Conference and Exhibit*, AIAA Paper 2007-5628, Cincinnati, Ohio, July 2007.

[12]Batterson, J. W., and Majdalani, J., "On the Viscous Bidirectional Vortex. Part 1: Linear Beltramian Motion," *46th AIAA/ASME/SAE/ASEE Joint Propulsion Conference and Exhibit*, AIAA Paper 2010-6763, Nashville, Tennessee, July 2010.

[13]Batterson, J. W., and Majdalani, J., "On the Viscous Bidirectional Vortex. Part 2: Noninear Beltramian Motion," *46th AIAA/ASME/SAE/ASEE Joint Propulsion Conference and Exhibit*, AIAA Paper 2010-6764, Nashville, Tennessee, July 2010.

[14]Batterson, J. W., and Majdalani, J., "Sidewall Boundary Layers of the Bidirectional Vortex," *Journal of Propulsion and Power*, Vol. 26, No. 1, 2009, pp. 102–112. doi:10.2514/1.40442.

[15]Morgan, A., "Possible Similarity Solutions of the Laminar, Incompressible, Boundary Layer Equations," *Transactions of the American Society of Mechanical Engineers*, Vol. 80, 1958, pp. 1559.

[16]Morgan, A., "The Reduction by One of the Number of Independent Variables in some Systems of Partial Differential Equations," *The Quarterly Journal of Mathematics*, Vol. 3, No. 1, 1952, pp. 250–259. doi:10.1093/qmath/3.1.250.

[17]Blasius, H., "Grenzschichten in Flüssigkeiten mit Kleiner Reibung," *Zeitschrift für Angewandte Mathematik und Physik (ZAMP)*, Vol. 56, 1908, pp. 1–37.

[18]Saad, T., and Majdalani, J., "Pressure Integration Rules and Restrictions for the Navier-Stokes Equations," *40th Fluid Dynamics Conference and Exhibit*, AIAA Paper 2010-4288, Chicago, Illinois, June 2010.

[19]Majdalani, J., and Chiaverini, M. J., "On Steady Rotational Cyclonic Flows: The Viscous Bidirectional Vortex," *Physics of Fluids*, Vol. 21, No. 10, 2009, pp. 103603. doi:10.1063/1.3247186.

[20]Murray, A., Gudgen, A., Chiaverini, M., Sauer, J., and Knuth, W., "Numerical Code Development for Simulating Gel Propellant Combustion Processes," *JANNAF*, May 2004.